Nanoscale Horizons

ROYAL SOCIETY OF CHEMISTRY

COMMUNICATION

View Article Online
View Journal | View Issue

Cite this: *Nanoscale Horiz.*, 2025, **10**, 2995

Received 30th April 2025,
Accepted 14th August 2025

DOI: 10.1039/d5nh00287g

rsc.li/nanoscale-horizons

Large piezo-/flexo-electric and flexomagnetic effects in a semiconducting cobalt telluride monolayer

Ying Liu,†[a] Wenfa Chen,†*[a] Yan Yin,[a] Ziming Tang,[a] Qihua Gong,*[ab] Min Yi[a] and Yanpeng Liu*[a]

Engineering piezo-/flexo-electricity and flexomagnetism in two-dimensional (2D) materials beyond the best-known graphene and transition metal dichalcogenides has potential for accelerating micro- and nano-electromechanical system applications. Herein, using first-principles calculations, we demonstrate cobalt monotelluride (CoTe) monolayer as an outstanding candidate for achieving large piezoelectric, flexoelectric and flexomagnetic responses down to the monolayer limit. The CoTe monolayer is found to be a semiconductor with a sizable bandgap of 0.48 eV, which is tunable using in-plane uniaxial or biaxial strains. This is because the puckered structure and intrinsic charge distribution asymmetry along the perpendicular direction enable the structure and properties to be heavily dependent on the external strain. In addition, the CoTe monolayer exhibits an out-of-plane polarization of up to ~21 pC m^{-1} with a flexoelectric coefficient of ~0.08 nC m^{-1} and a flexomagnetic coefficient of 89.59μ_B Å, surpassing most of the other 2D binary systems to the best of our knowledge. These findings not only clarify the fundamental structure and properties of the CoTe monolayer but also solidify the feasibility and designability of constructing piezo-/flexo-electric and flexomagnetic devices based on CoTe.

New concepts

The advances in nanotechnology have witnessed the explosive progress of two-dimensional cobalt telluride. However, most studies of two-dimensional cobalt telluride rely on experiments, and a systematical theoretical simulation to uncover the underlying versatile structure and properties is yet lacking, limiting the utilizations and developments of cobalt telluride. In this work, cobalt telluride is verified to become semiconducting if down-scaled from the metallic bulk form to the monolayer form. In addition, we found that the cobalt telluride monolayer exhibits robust electro-/magneto-mechanical behaviors, covering the remarkable piezoelectricity and strain gradient-related flexoelectricity and flexomagnetism. This research offers new understandings of cobalt telluride on a two-dimensional level and provides a promising prospect for designing cobalt telluride-based functional devices by strain gradient engineering.

1. Introduction

Structural symmetry is the core of the fascinating properties of 2D materials, and intentional or unintentional symmetry breaking introduces distinctive electronic and electro-/magneto-mechanical properties, such as the piezoelectric, flexoelectric and flexomagnetic effects.[1–4] From the viewpoint of a noncentrosymmetric structure with D_{3h} symmetry, transition metal dichalcogenides (TMDC) and transition metal dioxides (TMDO) with the chemical formula of MX_2 (where M = Cr, Mo, W, Ti, Zr, Hf, and Sn and X = O, S, Se, and Te) are theoretically predicted with piezoelectric coefficients lying in the range of ~0.3–1.0 nC m^{-1}.[5] To be more specific, the stretched MoS_2 monolayer, for example, computationally demonstrated a strong piezoelectric response of up to 0.368 nC m^{-1}.[6] This coefficient was later experimentally determined to be ~0.29 nC m^{-1},[7] which was comparable with that of traditional 3D α-quartz, AlN, and ZnO.[6,8] However, the piezoelectric field in these vdW layers is barely constricted within the basal plane and extremely hinders their applications.

Derived from traditional TMDCs, the Janus TMD monolayer (with the chemical formula MXY) sandwiches the transition metal layer between two distinct chalcogen layers, and the electronegativity differences of the X and Y atoms transform the space group from D_{3h} to C_{3v}. The vertical broken symmetry triggers the piezoelectric effect along the vertical operation mode that could be further enhanced by the interlayer-slidable Janus TMD bilayer and multilayers because of the dipole–dipole interaction between the adjacent vdW layers.[9–12] Similarly, group III

[a] *Key Laboratory for Intelligent Nano Materials and Devices of Ministry of Education, State Key Laboratory of Mechanics and Control for Aerospace Structures and Institute for Frontier Science, Nanjing University of Aeronautics and Astronautics, Nanjing 210016, China. E-mail: wfchen@nuaa.edu.cn, gongqihua@nuaa.edu.cn, chmliuyp@nuaa.edu.cn*

[b] *College of Physics, Nanjing University of Aeronautics and Astronautics, Nanjing 211106, China*

† Y. L. and W. C. contributed equally to this work.

monochalcogenides (for instance, GaS, GaSe, and InSe) have been simulated to be piezoelectric with piezoelectric stress coefficients of the same order of magnitude as that of the aforementioned MoS_2 monolayer.[13] Using machine learning on twelve different MA_2Z_4 (M = Cr, Mo, and W; A = Si and Ge; Z = N and P) monolayers, a class of sandwich structures that incorporated A atoms during the synthesis of the MZ_x crystals[14,15] exhibited remarkable piezoelectric coefficients, surpassing all the previously reported 2D materials.

In addition to the two-way coupling between the strain and polarization, the outstanding elastic modulus and tensile strengths enable the survival of 2D materials under the out-of-plane bending motion.[16] Spatial strain gradients tune the local polarization, thereby generating a flexoelectric response; such effects have been reported in the above-mentioned TMDCs, TMDOs, Janus TMDs, group III monochalcogenides, and MA_2Z_4 materials.[17] The co-existence of piezoelectricity and flexoelectricity within one crystallized material, especially at the 2D limit, holds promises for miniaturized nanoelectromechanical systems and nanoscale electronics. However, more 2D monolayers with superior piezo-/flexo-electricity still need to be developed, particularly in an easy and effective way.

Among the plentiful material candidates, 2D cobalt telluride (CoTe), a transition metal telluride with nearly exposed cobalt atoms, has been widely adopted in catalyst chemistry, solar cells, thermoelectrical and magnetic applications.[18,19] Initially, the rise of CoTe over the research horizon lied in its delicately tuned nanostructure and stoichiometric composition. Using well-established physical and chemical methods, such as pulsed laser deposition,[20] solvo-/hydro-thermal synthesis,[21] liquid-phase exfoliation,[22] chemical vapor transport[23] and chemical transformation routes,[24] CoTe nanodots, nanofilms, nanoflakes, nanotubes and nanorods were demonstrated as promising catalysts for the hydrogen/oxygen evolution reactions and related energy storage devices.[25,26] Another advantage of CoTe is the concurrence of metallic and (ferro-)magnetic behaviors. The saturation magnetization (M_s) of CoTe nanostructures was measured to be $\sim$13.4 emu g^{-1} at 2 K,[27] and a transition from superparamagnetic to ferromagnetic ordering was observed at room temperature ($M_s \sim$ 10.2–11.3 emu g^{-1}).[28] The vertically polarized charge distribution that enables the 2D CoTe monolayer to be a versatile platform for probing new physical phenomena, particularly structural distortion-induced effects like flexoelectricity and flexomagnetism, is highly important. Unfortunately, these topics remain largely unexplored till now, limiting the advancement of downstream devices.

In this work, we theoretically demonstrate the CoTe monolayer as a 2D semiconductor with outstanding piezo-/flexoelectric and flexomagnetic performances. The CoTe monolayer is first predicted to be semiconducting with a sizable bandgap. With respect to conventional 2D materials, the CoTe monolayer is intrinsically asymmetric along the vertical direction and more susceptible to external strain and strain gradient. Uniaxial or biaxial in-plane strains, for instance, are demonstrated to tune the band structure and bandgap. Along the out-of-plane direction, spontaneous polarization occurs, exhibiting outstanding piezoelectric properties. In addition, flexoelectric and flexomagnetic responses, *i.e.*, electric polarization and magnetic moment changes under a strain gradient, respectively, are produced. Our work shows the detailed structure and the excellent piezoelectric, flexoelectric and flexomagnetic properties of the CoTe monolayer and promotes the usage of the CoTe monolayer in advanced miniaturized devices and integrations.

Yanpeng Liu

Congratulations on the 10th anniversary. My bond with Nanoscale Horizons began in 2022 when I stood at the very start of my PI career. Amid many difficulties coupled with the COVID-19 pandemic, receiving the acceptance notice from Nanoscale Horizons filled me with an excitement and a great honor that remain vivid till now. We feel more grateful that another research advance is listed in this highly-reputed journal, especially in such a memorable collection. Best wishes to the Nanoscale Horizons since "there is plenty of room at the nanoscale".

2. Results and discussion

CoTe, a transition metal telluride, has a hexagonal crystal structure of tellurium with the cobalt atoms occupying the octahedral voids.[29] The bulk phase is nonmagnetic and metallic, while a bandgap is observed after lowering the dimensionality down to the 2D limit. In addition, the semiconducting CoTe monolayers exhibit intrinsic spin-polarized distributions of density of states (DOSs), demonstrating themselves as ideal material candidates for magnetic and spintronic applications. Next, we offer a systematic investigation of the CoTe monolayer from its atomic structure to unique properties, including electronic, piezoelectric, flexoelectric and flexomagnetic properties.

2.1. Structure and electronic properties

The optimized CoTe monolayer adopts a hexagonal lattice (space group *P3m*), in which each Co atom is coordinated to three Te atoms in a trigonal-pyramidal geometry and, conversely, each Te atom is coordinated to three Co atoms in a trigonal-pyramidal arrangement, forming a quasi-planar, atomically thin slab (Fig. 1a). The structure optimization yields a 2D CoTe unit cell with lattice parameters of $a = b = 4.39$ Å. In the top view (upper panel, Fig. 1a), Co and Te (stoichiometric ratio = 1 : 1) occupy alternating lattice sites of the honeycomb structure, while the side view (bottom panel, Fig. 1a) reveals a Te–Co–Te zigzag (ZZ) motif with a thickness of 0.67 Å.

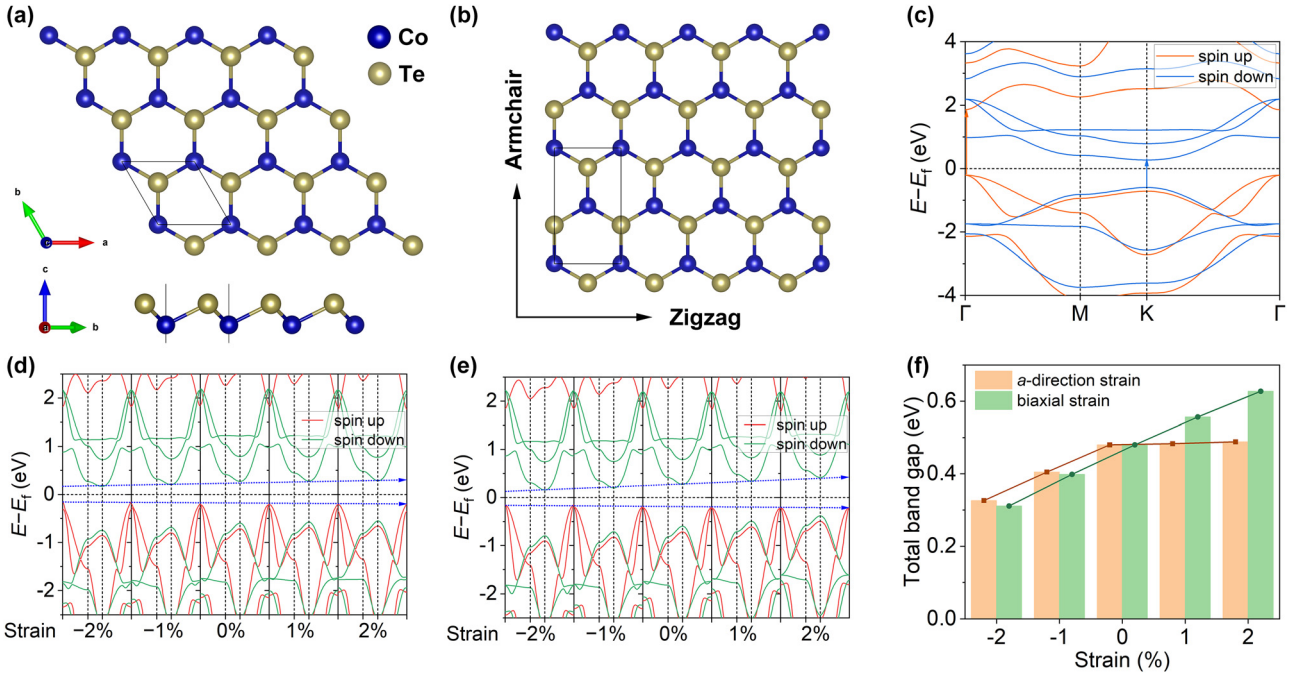

Fig. 1 Structure and electronic properties of the CoTe monolayer. (a) Top view (upper panel) showing the alternating Co/Te lattice sites, and side view (bottom panel) revealing the Te–Co–Te ZZ motif with a thickness of 0.67 Å. (b) Orthogonal unit cell (black solid rectangle) and crystallographic ZZ and AC directions. (c) Spin-polarized electronic band structure. (d) Bandgap evolution of the CoTe monolayer under varying uniaxial tensile strain. (e) Bandgap variation under biaxial tensile strain. (f) Comparison of the bandgap modulation by uniaxial and biaxial in-plane strains.

The orthogonal unit cell and two principal crystallographic directions—ZZ and armchair (AC)—are indicated in Fig. 1b.

The spin-polarized electronic band structure is calculated and shown in Fig. 1c. In contrast to the metallic character of its bulk counterpart,[18] the CoTe monolayer exhibits a direct bandgap of 2.07 eV for the spin-up states, with both the valence-band maximum (VBM) and conduction-band minimum (CBM) located at the Γ point. For the spin-down states, a direct bandgap of 0.89 eV is observed, with the VBM and CBM located at the K point. By considering the minimum difference between the VBM and CBM, regardless of the different spin states, the overall bandgap is 0.48 eV. It is worth noting that the density of states (DOSs) near the band edges are dominated by Co 3d and Te 5p states, indicating a strong Co–Te orbital hybridization (Fig. S1).

It is widely known that strain engineering offers an effective approach for tuning the bandgap of 2D monolayers.[30] For the CoTe monolayer, which belongs to the trigonal crystal system, we applied both uniaxial strain along the *a*-axis and biaxial strain to investigate their effects on the bandgap. Under a uniaxial tensile strain (ε) of up to 2% along the *a*-axis, with the *b*-axis held fixed, the bandgap changes monotonically. Specifically, the bandgap increases from 0.326 eV at $\varepsilon = -2\%$ to 0.488 eV at $\varepsilon = +2\%$ (Fig. 1d). Similarly, under a biaxial strain (ε_{bi}) applied simultaneously along both the *a*- and *b*-axis, the bandgap increases but with a higher sensitivity: from 0.311 eV at $\varepsilon = -2\%$ to 0.627 eV at $\varepsilon = +2\%$ (Fig. 1e). This comparison shows that the biaxial strain tunes the bandgap more effectively than the uniaxial strain, and the bandgap under biaxial strain is consistently higher across all the applied strain values. Furthermore, the change in the bandgap due to the biaxial strain is more pronounced, particularly for larger strain values (Fig. 1f), indicating that the CoTe monolayer exhibits a stronger response to the biaxial strain than to uniaxial strain.

To gain atomic-scale insights into the origin of this strain-induced band-gap modulation, we quantified the evolution of Co–Te bond lengths ($bond_1$–$bond_3$) and Te–Co–Te bond angles ($angle_1$–$angle_3$) under both uniaxial and biaxial strains from −2% to +2% (Table S1). Under uniaxial tension, $bond_1$ increases from 2.608 Å to 2.632 Å, $bond_2$ increases from 2.610 Å to 2.630 Å, and $bond_3$ increases from 2.611 Å to 2.630 Å; simultaneously, $angle_1$ expands from 111.12° to 116.70°, $angle_2$ shifts slightly from 114.49° to 113.18°, and $angle_3$ increases from 112.80° to 114.89°. Biaxial tension produces similar trends, with all the three bonds elongating by ∼0.012 Å and angles increasing by 0.9°–1.0°. These lattice distortions reduce the overlap between the Co 3d and Te 5p orbitals, weakening their hybridization and thereby directly contributing to the observed band-gap changes. We further carried out projected density of states (PDOS) analyses for the Co 3d and Te 5p orbitals at each strain point (Fig. S2). These calculations reveal that tensile strain shifts the Co 3d states upward in energy while weakening the contribution of Te 5p orbitals at the conduction-band minimum, driving the observed band-gap widening under tension and band gap narrowing under compression. Taken together, these results establish a direct correlation among the lattice distortions, orbital overlap, and electronic-structure modulation, providing a clear crystallographic and orbital-level mechanism for the strain-tuning behavior of the CoTe monolayer.

2.2. Piezoelectric properties

To evaluate the mechanical properties of the 2D CoTe monolayer, we calculated its elastic constants using the energy-strain method. In this approach, different strains are applied to the structure, and the total energy change relative to the ground-state energy (strain energy) is calculated for each distortion. The energy-strain relationship is then fitted using a second-order polynomial, from which the elastic constants are derived. To be more specific, the elastic tensor of the CoTe monolayer contains two independent elastic constants: C_{11} and C_{12} (see the SI). The mechanical stability criteria, given by $C_{11} > 0$ and $C_{11} > |C_{12}|$, are all satisfied, indicating the robust mechanical stability of the CoTe structure.

We further examined the mechanical properties of the CoTe monolayer by calculating the Young's modulus $Y(\theta)$, shear modulus $G(\theta)$, and Poisson's ratio $\nu(\theta)$, which are found to be isotropic across all the directions (Fig. 2a–c). The values obtained for these moduli are 3.8984 N m^{-1} for Young's modulus, 1.0339 N m^{-1} for shear modulus, and 0.8853 for Poisson's ratio (Table S2). These results indicate that the CoTe monolayer exhibits isotropic mechanical behavior, which means that its mechanical response is consistent across all the directions. Isotropic materials are particularly advantageous in applications such as in flexible electronics, sensors, and actuators that require uniform mechanical properties in all orientations for consistent performance across varying directions.

Next, we calculated the out-of-plane polarization strength (P_{out}) of the CoTe monolayer using the Berry phase method. Interestingly, the P_{out} of the CoTe monolayer is determined to be approximately 21 pC m^{-1}, enabling the CoTe monolayer to be one of the leading 2D materials (Fig. 2d) in terms of out-of-plane polarization; it substantially surpassed the reported values of many other 2D materials, such as SiSn, AlSb, and GeSn, and other well-studied 2D monolayers.[17,31–33]

To further assess the piezoelectric performance of the CoTe monolayer, we employed density functional perturbation theory. For two-dimensional systems, the piezoelectric tensor e_{ik}, elastic tensor C_{jk}, and piezoelectric coefficients d_{ij} are related as $e_{ik} = d_{ij} \cdot C_{jk}$. Our calculations yield an out-of-plane piezoelectric strain coefficient e_{31} of 26.2 pC m^{-1} for the CoTe monolayer, which is significantly higher than those of half-metallic Co_2Se_3 (9 pC m^{-1}), In_2Se_3 (11.9 pC m^{-1}) and $MoTe_2/In_2Se_3$ van der Waals heterostructures (17.9 pC m^{-1}).[17,34–37] More importantly, the out-of-plane piezoelectric strain coefficient d_{31} reaches 0.74 pm V^{-1}, surpassing the piezoelectric constants of most of the reported two-dimensional systems to date (Fig. 2e). The benchmark values for all the systems in the figure are strictly cited from the theoretical literature to highlight the exceptional theoretical performance of the CoTe monolayer. We emphasize that experimental validation of these high piezoelectric coefficients is crucial for translating this outstanding potential into practical nanoscale electromechanical devices.

2.3. Flexoelectric effect

When the CoTe monolayer is bent out-of-plane by applying a constant strain gradient (Fig. 3a and Fig. S3), *i.e.*, $\partial\varepsilon_{yz}/\partial y = 0.5\partial^2 u_z/\partial y^2 = 0.5$ K for AC bending and $\partial\varepsilon_{xz}/\partial x = 0.5\partial^2 u_z/\partial x^2 = 0.5$ K for ZZ bending, a change occurs in the out-of-plane polarization P_z. To offer more insights, we compute the P_z *via* the Berry-

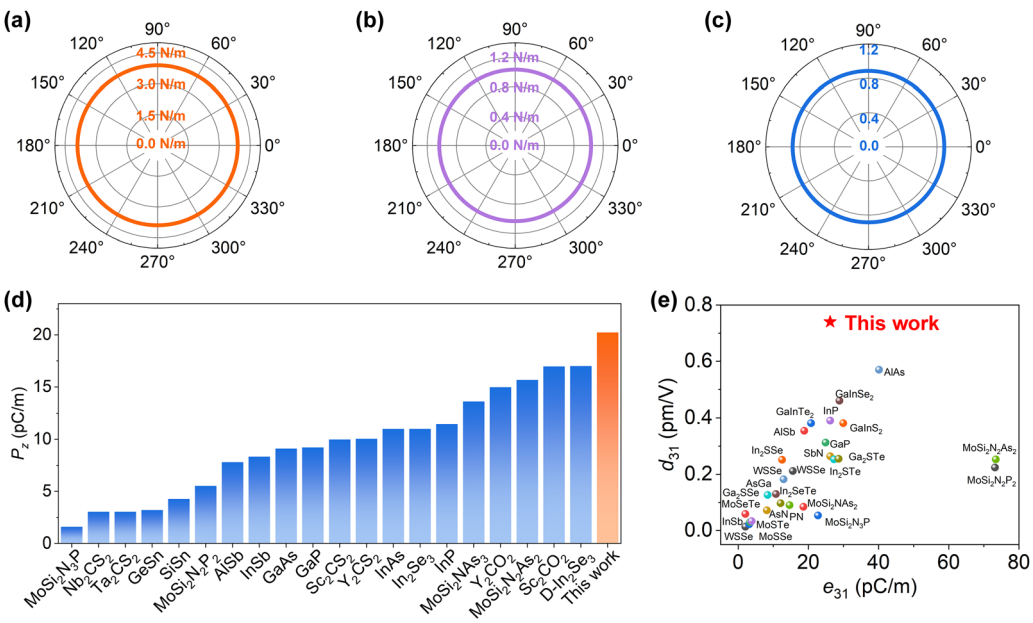

Fig. 2 Mechanical anisotropy and piezoelectric properties of the CoTe monolayer. (a)–(c) Polar diagrams of Young's modulus $Y(\theta)$ (orange), shear modulus $G(\theta)$ (purple) and Poisson's ratio $\nu(\theta)$ (blue) on the (001) plane. (d) Overview of the out-of-plane spontaneous polarization strength P_z of the CoTe monolayer compared with representative 2D materials. (e) Scatter plot of the out-of-plane piezoelectric stress coefficients d_{31} *versus* the out-of-plane piezoelectric strain coefficient e_{31} for CoTe and various 2D materials in their monolayer form; CoTe (red star) exhibits an exceptional d_{31} of 0.74 pm V^{-1} and a competitive e_{31} of 26.2 pC m^{-1}.

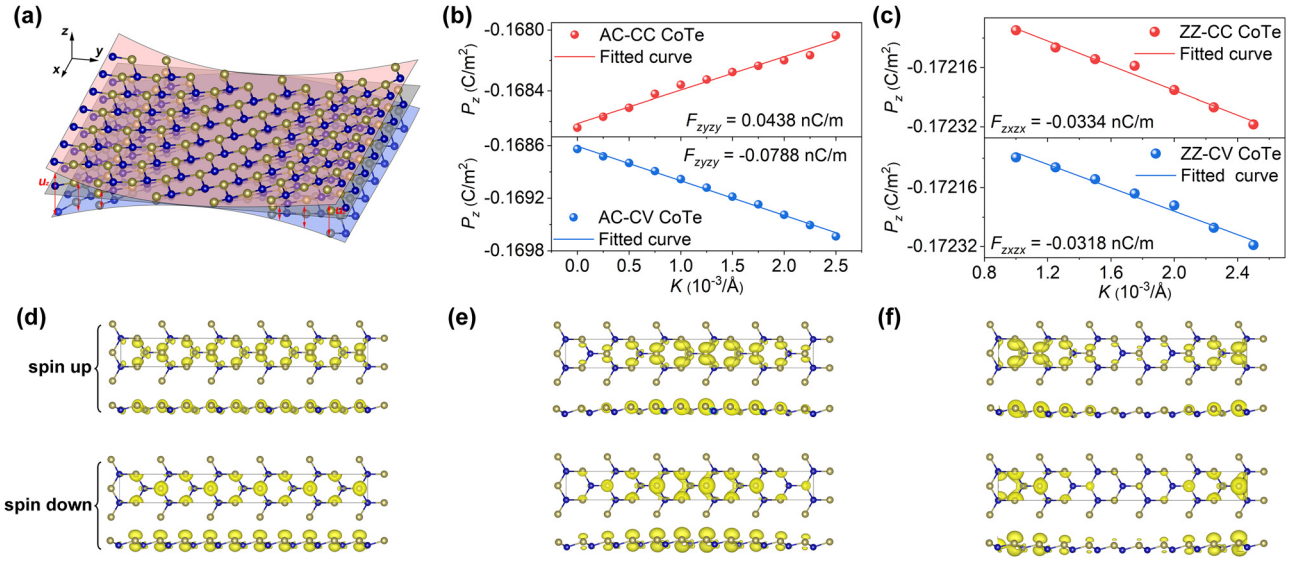

Fig. 3 Flexoelectric responses of the CoTe monolayer under out-of-plane bending with a constant shear-strain gradient. (a) Schematic of the CoTe monolayer bent with a constant shear-strain gradient K, defining AC (y) bending axis. Red arrows indicate the out-of-plane displacement profile $u_z(y)$. (b) Induced polarization P_z as a function of the strain gradient K for AC-CV (blue circles) and AC-CC (red circles) bendings. Solid lines represent linear fits. (c) Corresponding P_z–K curves for ZZ-CV (blue circles) and ZZ-CC (red circles) bendings, with fitted flexoelectric coefficients. (d)–(f) Partial charge density at the VBM for the spin-up (top) and spin-down (bottom) channels in a flat monolayer (d), under AC-CV bending (e), and under AC-CC bending (f). Panels (e) and (f) correspond to K = 0.0025 Å^{-1}.

phase approach for four bending geometries, *i.e.*, armchair-convex (AC-CV), armchair-concave (AC-CC), zigzag-convex (ZZ-CV) and zigzag-concave (ZZ-CC) and found that P_z scale strictly linearly with K in all the configurations (Fig. 3b and c). From the linear fits to the P_z–K data, we extract the flexoelectric coefficients as $F_{zyzy} = -0.079$ nC m^{-1} for AC-CV bending and +0.044 nC m^{-1} for AC-CC bending. Moreover, along the ZZ direction, we obtain $F_{zxzx} = -0.032$ nC m^{-1} for convex bending and -0.033 nC m^{-1} for concave bending. The larger magnitudes in the AC modes reflect their lower bending stiffness. In other words, the bending stiffness of the CoTe monolayer tends to be anisotropic with ratio up to $\sim$2.39.

At the atomic level (Fig. 3d–f), the out-of-plane bending with a constant shear-strain gradient breaks the uniform VBM charge distribution: under AC-CV bending, both the spin-up and spin-down densities shift toward the central convex region, generating a change in P_z, whereas under AC-CC bending, both the spin channels migrate to the concave edges. Meanwhile, the ZZ-CV bending and ZZ-CC bending yield the same qualitative redistribution. This strain gradient-driven charge asymmetry change at the band edge causes the observed $P_z \propto K$ relation.

For a more intuitive comparison, Table S2 lists the flexoelectric coefficients of the CoTe monolayer and those of the other reported binary two-dimensional materials. In the AC-CV mode, CoTe reaches $|F| \approx 0.08$ nC m^{-1}, which is nearly an order of magnitude larger than those of the prototypical TMDC monolayers (MoS_2: 0.0018; WS_2: 0.0016; $MoSe_2$: 6.9 $\times$ 10^{-4}; WSe_2: 7.6 $\times$ 10^{-4}; $MoTe_2$: 0.0023; and WTe_2: 0.0020 nC m^{-1}) and even exceeds the values of some functionalized graphene ribbons (CH: 0.035 and CF: 0.062 nC m^{-1}). In a nutshell, the CoTe monolayer exhibits the strongest flexoelectric response among these binary 2D systems, which is promising for modern-day electromechanical transductions at a 2D limit.

2.4. Dipole responses and flexomagnetic properties

We then quantified the dipole moment change $\Delta\mu$ of the four bent CoTe geometries, AC-CC (Fig. 4a), AC-CV (Fig. 4b), ZZ-CC (Fig. 4c) and ZZ-CV (Fig. 4d), under a range of strain gradient values K and perpendicular electric fields. For the AC-CC geometry, $\Delta\mu_z$ displays minimal variation as the field sweeps from negative to positive, regardless of K. In contrast, in AC-CV, ZZ-CC and ZZ-CV, $\Delta\mu_z$ becomes progressively more negative with increasing field, and the degree of this negative shift increases with the larger curvature values of K, indicating a curvature-amplified suppression of the dipole moment along both the AC and ZZ directions.

Spin-resolved partial charge densities at the VBM (red isosurfaces) and CBM (green isosurfaces) under a field of 0.5 eV Å^{-1} (Fig. 4e) confirm the net electron displacement toward negative z-axis, which is consistent with the $\Delta\mu_z$ trend across the bending modes. Finally, we evaluated the flexomagnetic behavior by tracking the unit-cell magnetic moment upon bending. As shown in Fig. 4f, for the AC-CV bent structure, the magnetic moment decreases from 2.45 μ_B for the initially flat monolayer to 2.22μ_B under mechanical curvature, corresponding to a large flexomagnetic coefficient around 89.59μ_B Å. Therefore, it is verified that a strain gradient can effectively tune the magnetization of the CoTe monolayer.

3. Conclusions

In conclusion, we provide a comprehensive study of the 2D cobalt telluride monolayer using theoretical calculations.

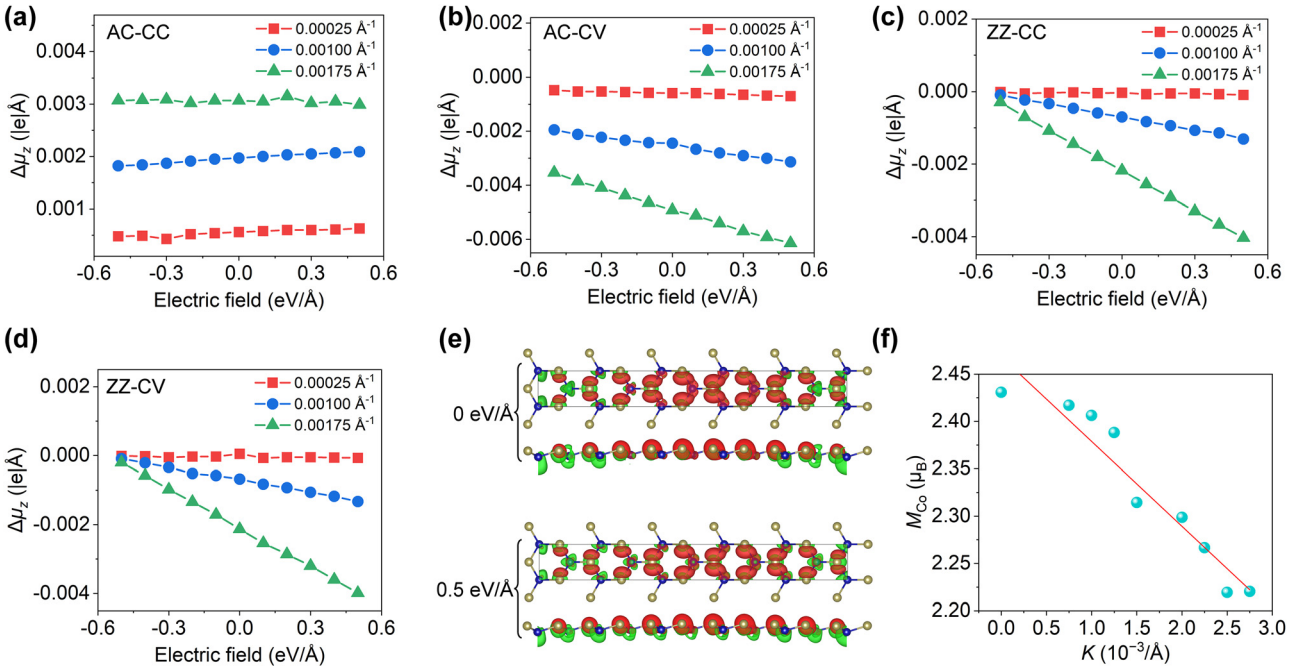

Fig. 4 Dipole and flexomagnetic responses. (a)–(d) Change in the dipole moment ($\Delta\mu_z$) as a function of the electric field for AC-CC, AC-CV, ZZ-CC and ZZ-CV bends at K = 0.00025, 0.00100 and 0.00175/Å, respectively. The AC-CC geometry shows minimal $\Delta\mu_z$ variation, while AC-CV, ZZ-CC and ZZ-CV exhibit more negative $\Delta\mu_z$ with increasing curvature. (e) Top and side views of the spin-up charge densities (VBM, red; CBM, green) for AC-CV at K = 0.00175/Å without field (top) and with a 0.5 eV Å^{-1} field (bottom). (f) Magnetic moment plotted against the strain gradient.

Differentiating from its bulk counterpart, the CoTe monolayer becomes semiconducting with a bandgap of ~0.48 eV. The bandgap could be tuned by uniaxial or biaxial in-plane strains, and it monotonically increases with increments in tensile stress. More importantly, the CoTe monolayer is predicted to exhibit an exceptionally high out-of-plane polarization of up to ~21 pC m^{-1}, ranking top in the 2D piezoelectrics developed to date. The flexoelectric coefficients of the CoTe monolayer is calculated to be 0.08 nC m^{-1}, which is almost one order of magnitude larger than those of the conventional TMDC monolayers. The pristine CoTe monolayer is found to be flexomagnetic with a coefficient of 89.59μ_B Å that could be manifested by strain gradient engineering. We believe that this work not only offers insightful guidance for newcomers but also promulgates the great potentials of the CoTe monolayer toward diverse electromechanical devices.

4. Computational methods

All density functional theory (DFT) calculations were performed using the Vienna *ab initio* simulation package (VASP),[38,39] employing the projector-augmented wave (PAW) method[40] in conjunction with the Perdew–Burke–Ernzerhof (PBE) exchange–correlation functional.[41] The ion-electron interactions were modeled using PAW pseudopotentials, with a plane-wave energy cutoff of 520 eV. The electronic convergence criterion was set at 10^{-8} eV for self-consistent field (SCF) iterations. Geometric optimizations were carried out using the conjugate gradient algorithm, with atomic forces converging below 0.001 eV Å^{-1}. For the optimization of the 2D CoTe unit cell, Brillouin zone integrations were performed using Monkhorst–Pack k-point meshes of 15 × 15 × 1. A vacuum spacing of more than 20 Å in the z-direction was included in all the models to prevent artificial interactions due to periodic boundary conditions. The Co U value used in the calculations was set at 5 eV in the DFT+U method to account for the strong correlation effects in the Co 3d orbitals.

The dipole moment was calculated using the Berry phase method.[42,43] The effective thickness of the 2D CoTe used in this work corresponded to the vertical distance between the Co and Te atoms along the z-axis. The AC direction was expanded with a 1 × 5 × 1 supercell, while the ZZ direction was expanded with a 10 × 1 × 1 supercell. Curved structures of 2D CoTe were constructed by displacing the atomic z-coordinates according to a quadratic function ($u_z = (K/2)\cdot x^2$ or $u_z = (K/2)\cdot y^2$), where K is the strain gradient of the curved plane, defined as $K = \partial^2 u_z/\partial x^2$ or $K = \partial^2 u_z/\partial y^2$. These curved geometries were generated using a custom Python program, and subsequent relaxation calculations were performed using DFT simulations.

As outlined in previous studies, the applied bending perturbations induced only the xz or yz strain components and their strain gradient terms ($\partial\varepsilon_{xz}/\partial x$ or $\partial\varepsilon_{yz}/\partial y$), while the other components of the strain and strain gradient tensors remained zero. The total induced polarization (P_z) can thus be expressed along the z-direction as follows:

$$P_z = d_{zxz}\varepsilon_{xz} + F_{zxzx}\partial\varepsilon_{xz}/\partial x \text{ or } P_z = d_{zyz}\varepsilon_{yz} + F_{zyzy}\partial\varepsilon_{yz}/\partial y.$$

Additionally, the angle-dependent Young's modulus $Y(\theta)$, shear modulus $G(\theta)$, and Poisson's ratio $\nu(\theta)$ were calculated using the elastic constants *via* the VASPKIT software.

Author contributions

All authors have given approval to the final version of the manuscript.

Conflicts of interest

The authors declare no conflict of interest.

Data availability

The datasets generated during and/or analyzed during this study are available from the authors on reasonable request.

Supplementary information includes PDOS (Fig. S1), bending schematic (Fig. S2), and mechanical-property ranges (Tables S1 and S2). See DOI: https://doi.org/10.1039/d5nh00287g.

Acknowledgements

The authors wish to acknowledge the financial support provided by the National Natural Science Foundation of China (Grant No. 12372111, 12302134, 11902150, 12272173), National Key Research and Development Program of China (2019YFA0705400), Natural Science Foundation of Jiangsu Province (Grant No. BK20210312), China Postdoctoral Science Foundation (2023M741690), Fundamental Research Funds for the Central Universities and the State Administration of Science, Technology and Industry for National Defense (NE2023006, NS2023054, NC2023001, NJ2023002, NJ2022002, ILF23010, THB24004), Program for Innovative Talents and Entrepreneur in Jiangsu, Research Fund of State Key Laboratory of Mechanics and Control of Mechanical Structures (MCMS-I-0422K01), National Youth Talents Program of China and a project funded by the Priority Academic Program Development of Jiangsu Higher Education Institutions. This work is partially supported by High Performance Computing Platform of Nanjing University of Aeronautics and Astronautics. Thanks to the Center for Microscopy and Analysis (NUAA) for the technical assistance.

References

1 S. Manzeli, D. Ovchinnikov, D. Pasquier, O. Yazyev and A. Kis, *Nat. Rev. Mater.*, 2017, **2**, 1–15.
2 L. Du, T. Hasan, A. Castellanos-Gomez, G. Liu, Y. Yao, C. Lau and Z. Sun, *Nat. Rev. Phys.*, 2021, **3**, 193–206.
3 Z. Tang, Q. Gong and M. Yi, *Mater. Sci. Eng., R*, 2025, **162**, 100878.
4 Q. Gong, Z. Tang and M. Yi, *Phys. Rev. B*, 2025, **111**, 094441.
5 M. Alyoruk, Y. Aierken, D. Çakır, F. Peeters and C. Sevik, *J. Phys. Chem. C*, 2015, **119**, 23231–23237.
6 K. Duerloo, M. Ong and E. Reed, *J. Phys. Chem. Lett.*, 2012, **3**, 2871–2876.
7 A. Lu, H. Zhu, J. Xiao, C. Chuu, Y. Han, M. Chiu, C. Cheng, C. Yang, K. Wei, Y. Yang and Y. Wang, *Nat. Nanotechnol.*, 2017, **12**, 744–749.
8 W. Wu and Z. Wang, *Nat. Rev. Mater.*, 2016, **1**, 1–17.
9 L. Dong, J. Lou and V. Shenoy, *ACS Nano*, 2017, **11**, 8242–8248.
10 H. Cai, Y. Guo, H. Gao and W. Guo, *Nano Energy*, 2019, **56**, 33–39.
11 X. Tang and L. Kou, *Phys. Status Solidi (b)*, 2022, **259**, 2100562.
12 X. Zhang, Y. Cui, L. Sun, M. Li, J. Du and Y. Huang, *J. Mater. Chem. C*, 2019, **7**, 13203–13210.
13 W. Li and J. Li, *Nano Res.*, 2015, **8**, 3796–3802.
14 T. Rabczuk, X. Zhuang, B. Mortazavi, B. Javvaji, F. Shojaei and A. Shapeev, *Nano Energy*, 2021, **82**, 105716.
15 Y. Hong, Z. Liu, L. Wang, T. Zhou, W. Ma, C. Xu, S. Feng, L. Chen, M. Chen, D. Sun and X. Chen, *Science*, 2020, **369**, 670–674.
16 Y. Yin, Q. Gong, M. Yi and W. Guo, *Mater. Horiz.*, 2023, **10**, 5177–5184.
17 Y. Yin, Q. Gong, M. Yi and W. Guo, *Adv. Funct. Mater.*, 2023, **33**, 2214050.
18 Y. Liu, Q. Gong, Y. Yin, M. Yi and Y. Liu, *Adv. Funct. Mater.*, 2024, **34**, 2310372.
19 K. Burch, D. Mandrus and J. Park, *Nature*, 2018, **563**, 47–52.
20 Z. Zhang, W. Hines and J. Budnick, *AIP Adv.*, 2017, **7**, 125322.
21 M. Manikandan, K. Subramani and M. Sathish, *RSC Adv.*, 2020, **10**, 13632–13641.
22 S. Demiss, R. Tromer and S. Siddique, *Appl. Phys. A: Mater. Sci. Process.*, 2022, **128**, 379.
23 D. Wang, F. Luo and M. Lu, *Small*, 2019, **15**, 1804404.
24 H. Ma, W. Dang and X. Yang, *Chem. Mater.*, 2018, **30**, 8891–8896.
25 Q. Gao, C. Huang and Y. Ju, *Angew. Chem., Int. Ed.*, 2017, **56**, 7769–7773.
26 X. Cao, J. Medvedeva and M. Nath, *ACS Appl. Energy Mater.*, 2020, **3**, 3092–3103.
27 R. Shi, X. Liu, Y. Shi, R. Ma, B. Jia, H. Zhang and G. Qiu, *J. Mater. Chem.*, 2010, **20**, 7634–7636.
28 M. Malagutti, K. de Fátima Ulbrich, V. Paes, J. Geshev and C. de Campos, *RSC Adv.*, 2021, **11**, 5027–5034.
29 E. Uchida, *J. Phys. Soc. Jpn.*, 1955, **10**, 517–522.
30 X. Nie, X. Wu, Y. Wang, S. Ban, Z. Lei, J. Yi, Y. Liu and Y. Liu, *Nanoscale Horiz.*, 2023, **8**, 158–175.
31 K. Lee and C. Lee, *Sci. Rep.*, 2020, **10**, 11300.
32 A. Samad, H. Kim and Y. Shin, *J. Phys.: Condens. Matter*, 2018, **31**, 045301.
33 C. Yao, H. Huang, Y. Yao, Y. Wu and X. Hao, *J. Phys.: Condens. Matter*, 2021, **33**, 145302.
34 W. Ding, J. Zhu, Z. Wang, Y. Gao, D. Xiao, Y. Gu, Z. Zhang and W. Zhu, *Nat. Commun.*, 2017, **8**, 14956.
35 C. Tang, L. Zhang, D. Wijethunge, K. K. Ostrikov and A. Du, *J. Phys. Chem. C*, 2021, **125**, 24648–24654.
36 Y. Chen, Z. Tang, H. Shan, B. Jiang, Y. Ding, X. Luo and Y. Zheng, *Phys. Rev. B*, 2021, **104**, 075449.
37 Y. Li, D. Legut, X. Liu, C. Lin, X. Feng, Z. Li and Q. Zhang, *J. Phys. Chem. C*, 2022, **126**, 8817–8825.
38 J. Hafner, *Comput. Phys. Commun.*, 2007, **177**, 6–13.

39 J. Hafner, *J. Comput. Chem.*, 2008, **29**, 2044–2078.
40 P. E. Blöchl, *Phys. Rev. B: Condens. Matter Mater. Phys.*, 1994, **50**, 17953–17979.
41 J. P. Perdew, K. Burke and M. Ernzerhof, *Phys. Rev. Lett.*, 1996, **77**, 38653868.
42 R. Resta, *J. Phys.: Condens. Matter*, 2002, **14** R625–R656.
43 T. Xu, J. Zhang, Y. Zhu, J. Wang, T. Shimada, T. Kitamura and T. Y. Zhang, *Nanoscale Horiz.*, 2020, **5**, 1400–1406.